Harmonic Generation Using Nonlinear *LC* Lattices

Georgios N. Lilis, *Member, IEEE*, Jihyuk Park, Wooram Lee, *Student Member, IEEE*, Guansheng Li, Harish S. Bhat, and Ehsan Afshari, *Member, IEEE*

***Abstract*—Nonlinear *LC* lattices have shown promise for high-power high-frequency signal generation. Here we offer the first detailed study of the frequency response of these lattices, as well as a method designed to find input excitation frequencies that result in intense harmonic generation. The crux of the method is to locate regions in frequency space where the spectral norm of the lattice response matrix is large. When the fundamental excitation frequency (or one of its multiples) is located in these regions, the lattice harmonic response is intensified. These findings are supported by extensive numerical simulations and experimental measurements. We deal chiefly with a first-order dependency of capacitance (*C*) on voltage (*V*); however, it is also shown that lattices with higher order *C–V* dependencies achieve proportionally higher harmonic generation. Simulations using a 0.13-μm CMOS process indicate harmonic generation at 400 GHz (three times the cutoff frequency of the fastest active device in this process), suggesting potential applications of this lattice topology in terahertz range devices.**

***Index Terms*—Inductor–capacitor lattices, nonlinear transmission lines, solitons, terahertz frequency generation.**

I. Introduction

LATELY there has been increasing interest in implementing devices operating in the terahertz frequency band (100 GHz–10 THz) [1] with exciting potential applications in a variety of areas such as spectroscopy [2], imaging [3], and communications [4]. However, it is quite challenging to generate powerful terahertz signals in today's commercial CMOS processes, given that the maximum operating frequencies of most MOS transistors range between 200–300 GHz.

To go beyond the frequency limit imposed by active devices, people resort to nonlinear passive structures, which are capable of generating high-order harmonics of the input signals [5]. An extensively studied example is the nonlinear transmission line [6], which (in the most popular version), consists of inductors and voltage-dependent capacitors (varactors [7], [8]) [9]–[17] and has been implemented using Schottky barrier strip lines [18], micromachined waveguides [19], as well as using structures on GaAs [20]–[23], InP [24], and Si [25] substrates. However, due to loss and limited input power, the high-frequency components in the output are usually small.

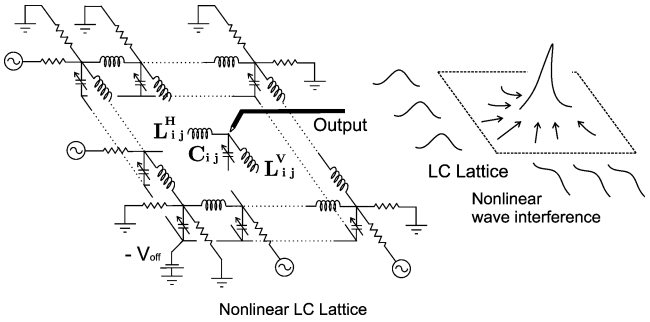

Fig. 1. Nonlinear *LC* lattice.

To achieve high power at high frequencies, we study a 2-D nonlinear *LC* lattice, as shown in Fig. 1. This lattice is a foursquare periodic structure [26], consisting of identical inductors and voltage-dependent capacitors. It is excited by sinusoidal voltage sources on two sides of its boundary and terminated with a matched load on the other two sides.

Nonlinear wave propagation in similar 2-D topologies involving different types of nonlinearities has been studied in the past. Examples include: lattices with second-order voltage-dependent capacitive elements analyzed using the Kadomtsev–Petviashvili (KP) equation [27], Toda lattices exhibiting logarithmic nonlinearities [28], [29], and coupled nonlinear transmission lines with general polynomial nonlinearities [30]–[32].

Recent theoretical work in 2-D nonlinear lattices with first-order capacitance–voltage dependencies [33], [34] demonstrated how constructive interference enables in-phase waves to combine and produce outgoing waves with much larger peak-to-peak amplitudes than the ones measured in linear equivalents. Furthermore, experimental work verified that these lattices support Cerenkov radiation and soliton resonance phenomena [35], [36].

In previous work demonstrating the potential utility of nonlinear *LC* lattices for high-frequency signal generation, the frequency response of these lattices was not studied. Here we solve this problem; by studying in detail the frequency response, we develop the intense harmonic generation (IHG) method, which can be used to find input excitation frequencies that result in IHG. A feature of the IHG method is that it can be applied to study 2-D lattices with polynomial capacitance–voltage dependencies of arbitrary order, which are not well-understood in general.

Manuscript received May 04, 2009; revised February 25, 2010; accepted April 15, 2010. Date of publication May 24, 2010; date of current version July 14, 2010. This work was supported by the C2S2 Focus Center, one of six research centers funded under the Focus Center Research Program (FCRP), a Semiconductor Research Corporation entity. The work of W. Lee was supported under a Samsung Fellowship. The work of H. S. Bhat was supported in part by the National Science Foundation (NSF) under NSF Grant DMS-0753983. The work of E. Afshari was supported by the NSF under NSF Grant DMS-0713732 and under CAREER Award 0954537.

G. N. Lilis, J. Park, W. Lee, G. Li, and E. Afshari are with the Department of Electrical and Computer Engineering, Cornell University, Ithaca, NY 14850 USA (e-mail: gnl2@cornell.edu; jp399@cornell.edu; wl287@cornell.edu; gl246@cornell.edu; ehsan@ece.cornell.edu).

H. S. Bhat is with the School of Natural Sciences, University of California, Merced, CA 95343 USA (e-mail: hbhat@ucmerced.edu).

Color versions of one or more of the figures in this paper are available online at http://ieeexplore.ieee.org.

Digital Object Identifier 10.1109/TMTT.2010.2049678

This paper is organized as follows. Section II contains the modeling of the lattice behavior and the study of its frequency response. The section concludes with the description of the IHG method. Section III contains the verification of the IHG method using extensive MATLAB simulations and experimental measurements of a real lattice implemented on printed circuit board (PCB). This paper resumes in Section IV, where an implementation with a 0.13-μm CMOS process is presented. It is shown by simulation using Cadence Spectre that this lattice topology supports IHG at terahertz frequencies.

II. Nonlinear Lattice Model and IHG Method

A. Preliminaries

In this paper, an $N \times N$ square lattice is studied, the cells of which are identical. Each cell consists of one nonlinear capacitor and two identical inductors, as displayed in Fig. 1. A first-order approximation is used to model the capacitance–voltage dependence of the nonlinear capacitors, i.e.,

$$C_{i,j}(V_{i,j}) = C_o(1 - bV_{i,j}) \tag{1}$$

where C_o is the capacitance at zero voltage, b is a constant, and $C_{i,j}$ is the capacitance of the i, j cell at voltage $V_{i,j}$. Although this approximation is adopted here for simplicity, higher order dependencies can be studied in a similar manner.

By Kirchhoff's Law, the time-domain behavior of this lattice can be described as follows:

$$[E]\left\{\frac{\partial s}{\partial t}\right\} = [F]\{s\} + \{x\} + b[C]\{s\}.\left\{\frac{\partial s}{\partial t}\right\} \tag{2}$$

in which state vector $\{s\}$ consists of the capacitor voltages and the inductor currents, matrix $[E]$ contains the zero-biased capacitances C_o, and inductance, matrix $[C]$ contains the zero-biased capacitances C_o only, matrix $[F]$ describes the interconnections of the lattice elements, as well as inductor's ohmic losses, and vector $\{x\}$ contains the input signals. The "." notation indicates element-wise multiplication. (For additional details, consult the Appendix.)

By applying the Fourier transform on both sides of (2), one obtains the frequency-domain description of the lattice

$$[j(2\pi f)E]\{\hat{s}\} = [F]\{\hat{s}\} + \{\hat{x}\} + b[C]\{\hat{s}\} * \{j(2\pi f)\hat{s}\} \tag{3}$$

where $\hat{\cdot}$ represents the frequency-domain variables and "$*$" denotes element-wise convolution. Solving the above system perturbatively, we derive the frequency response

$$\{\hat{s}\} = \{\hat{s}_0\} + b\{\hat{s}_1\} + b^2\{\hat{s}_2\} + \cdots \tag{4}$$

with

$$\begin{aligned}
\{\hat{s}_0\} &= [M(f)]^{-1}\{\hat{x}\} \\
\{\hat{s}_n\} &= [M(f)]^{-1}\{\hat{c}_n\}, \qquad n = 1, 2, \ldots \\
\{\hat{c}_n\} &= [C]\sum_{k=0}^{n-1}\{\hat{s}_k\} * \{j(2\pi f)\hat{s}_{n-1-k}\} \\
[M(f)] &= j(2\pi f)[E] - [F].
\end{aligned} \tag{5}$$

B. Lth-Order Capacitance–Voltage Dependencies

A similar approach can be used for the harmonic analysis of lattices with varactors satisfying an Lth-order capacitance–voltage relation

$$C_{i,j}(V_{i,j}) = C_o\left(1 - \sum_{\ell=1}^{L} b_\ell V_{i,j}^{\ell}\right). \tag{6}$$

In this case, the nonlinear part of the state equation $\{\hat{n}\}$ contains multiconvolutions instead of the convolution pairs contained in (3)

$$\begin{aligned}
[j(2\pi f)E]\{\hat{s}\} &= [F]\{\hat{s}\} + \{\hat{x}\} + \{\hat{n}\} \\
\{\hat{n}\} &= \sum_{\ell=1}^{L} b_\ell [C]\underbrace{\{\hat{s}\} * \cdots * \{\hat{s}\}}_{\ell \text{ times}} * \{j(2\pi f)\hat{s}\}.
\end{aligned} \tag{7}$$

Using a multidimensional perturbative method, the solution of (7) can be expressed as a series of solutions indexed by a vector $\bar{\ell} = \{\ell_1, \ldots, \ell_L\}$

$$\{\hat{s}\} = \sum_{\bar{\ell} \in \mathbb{N}^L} (b_1^{\ell_1} \cdots b_L^{\ell_L})\{\hat{s}_{\bar{\ell}}\}. \tag{8}$$

Substituting (8) in (7) and equating with zero the coefficients of the terms $(b_1^{\ell_1} \cdots b_L^{\ell_L})$ leads to the solution of (7), obtained in a recursive manner, shown in (9) at the bottom of this page.

C. Harmonic Generation

The convolutions in the solutions (5) and (9) are responsible for harmonic generation appearing in the nonlinear parts of the

$$\begin{aligned}
\{\hat{s}_{\bar{0}}\} &= [M(f)]^{-1}\{\hat{x}\}, \qquad \bar{0} = \{\overbrace{0, \ldots 0}^{L \text{ times}}\} \\
\{\hat{s}_{\bar{\ell}}\} &= [M(f)]^{-1}\{\hat{c}_{\bar{\ell}}\}, \qquad \bar{\ell} \in \mathbb{N}^L \backslash \{\bar{0}\} \\
\{\hat{c}_{\bar{\ell}}\} &= [C] \sum_{\sum_{i=1}^{m} \bar{k}_i = \bar{\ell} - \bar{e}_m} \{\hat{s}_{\bar{k}_1}\} * \cdots * \{\hat{s}_{\bar{k}_{m-1}}\} * \{j(2\pi f)\hat{s}_{\bar{k}_m}\} \\
[M(f)] &= j(2\pi f)[E] - [F], \qquad \bar{e}_m = \{0, \ldots, \underbrace{1}_{m\text{th position}}, \ldots 0\}
\end{aligned} \tag{9}$$

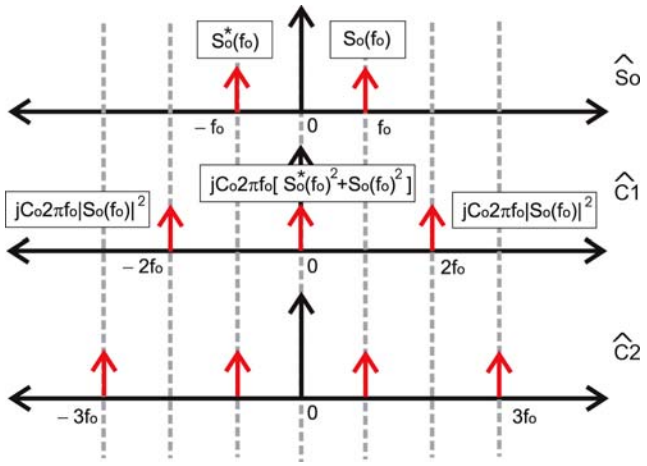

Fig. 2. Harmonic generation example.

state (voltage/current) vectors $\{\hat{s}_n\}, n = 1, 2, \ldots$ and $\{\hat{s}_{\bar{l}}\}, \bar{l} \in \mathbb{N}^L \backslash \{\bar{0}\}$, respectively. This phenomenon is called spectrum expansion and is illustrated in the plot of Fig. 2 for the case of first-order capacitance–voltage dependent varactors. More precisely: for a sinusoidal voltage input $\{\hat{x}\}$, the linear response $\{\hat{s}_o\}$ is a sinusoidal signal at the fundamental frequency; by convolution, a dc component and a second harmonic are generated in $\{\hat{c}_1\}$; then, again by convolution, the third harmonic appears in $\{\hat{c}_2\}$. The other high-order harmonics are generated in a similar way. Similar conclusions can be drawn using (9) for Lth-order capacitance–voltage dependencies with $L > 1$. In these cases, as the order L and the respective coefficients b_ℓ (with $\ell \leq L$) become larger, the achieved spectrum expansion increases proportionally, due to multistage convolutions in (9). As a simple example, the harmonics generated by $\{\hat{c}_1\} = \{\hat{s}_0\} * \{j(2\pi f)\hat{s}_0\}$ when $L = 1$ reach at most $\pm 2f_0$ (see Fig. 2). This should be compared with the harmonics generated by an $L = 2$ case where $\{\hat{c}_{01}\} = \{\hat{s}_{00}\} * \{\hat{s}_{00}\} * \{j(2\pi f)\hat{s}_{00}\}$ expands the spectrum of the solution of (9) to $\pm 4f_0$.

Based on this harmonic generation mechanism, solution (5) can be expressed as a summation of a dc component $\{\hat{h}_0\}$, a fundamental $\{\hat{h}_1\}$, and different harmonics $\{\hat{h}_n\}, n > 2$

$$\{\hat{s}\} = \{\hat{h}_0\} + \{\hat{h}_1\} + \{\hat{h}_2\} + \cdots \tag{10}$$

with

$$\{\hat{h}_0\} = [M(0)]^{-1} \sum_{n=1,3,\ldots} b^n \{\hat{c}_n(0)\} \tag{11a}$$

$$\{\hat{h}_1\} = [M(f_0)]^{-1} \left[\{\hat{x}\} + \sum_{n=2,4,\ldots} b^n \{\hat{c}_n(f_o)\} \right] \tag{11b}$$

$$\{\hat{h}_2\} = [M(2f_0)]^{-1} \sum_{n=1,3,\ldots} b^n \{\hat{c}_n(2f_o)\} \tag{11c}$$

$$\{\hat{h}_3\} = [M(3f_0)]^{-1} \sum_{n=2,4,\ldots} b^n \{\hat{c}_n(3f_o)\} \tag{11d}$$

and so on for $\hat{h}_k$ for $k \geq 4$. The harmonic performance of the lattice, when excited by a fundamental frequency f_0, can be evaluated by measuring the harmonic energy $H(f_0)$, which is defined as the sum of the second norms of the harmonic vectors $\|\hat{h}_k\|_2, k = 2, 3, \ldots$

$$H(f_0) = \sum_{k=2}^{K} \|\hat{h}_k\|_2^2. \tag{12}$$

D. Spectral Norm Analysis

The harmonic expansion (10), as well as similar expansions of (9) for the case of Lth-order capacitance–voltage dependencies, suggest that the matrices $[M(kf_0)]^{-1}$, $k = 0, 1, 2, \ldots$ play an important role in determining the energy of the kth harmonic vector $\{\hat{h}_k\}$ expressed by the square of its second norm $\|\hat{h}_k\|_2^2$ in (12). The harmonic vectors $\{\hat{h}_k\}$ are calculated by the multiplication of the matrix $[M(kf_0)]^{-1}$ with the convolution vectors $\sum_n b^n \{\hat{c}_n(kf_0)\}$, which also involve multiplications of the matrices $[M(kf_0)]^{-1}$, $k = 1, 2, \ldots$ with the constant input vector $\{\hat{x}\}$, according to (5). The frequencies f_0 at which the multiplication of a vector $\{x\}$ with the matrices $[M(kf_0)]^{-1}$, $k = 1, 2, \ldots$ results in a vector of higher energy (with the energy of a vector $\{x\}$ expressed as the square of its second norm $\|x\|_2^2$) are the ones at which the spectral norm of $[M(kf_0)]^{-1}$, $k = 1, 2, \ldots$ is maximized.[1] Consequently, since the harmonic vectors in (11a)–(11d) are obtained by multiplications of $[M(kf_0)]^{-1}$, higher values of the spectral norm of $[M(f)]^{-1}$ at the fundamental f_0 or its harmonics kf_0 lead to a more intense harmonic boost. Following these ideas, the IHG method (presented in Section II-E) uses a plot of the spectral norm of $[M(f)]^{-1}$ with respect to f in order to identify the fundamentals f_0, which result in intense harmonic boost.

As an example, consider Fig. 3, which shows a plot of the spectral norm of $[M(f)]^{-1}$ for a lattice with parameters specified by Table I. This plot indicates that there are two desirable frequency bands in which the spectral norm is locally maximized: Low: 40–42 MHz and High: 54–57 MHz.

Two intertwined factors affecting the spectral norm values of $[M(f)]^{-1}$ are: 1) the ohmic loss of the lattice inductors (r) and 2) the lattice size (N) appearing in the matrix $[F]$ [a component of $[M]$ according to (5)]. As the ohmic losses of the inductors increase, or as the lattice size decreases, the regions of local maxima of the spectral norm—which correspond to frequency bands at which intense harmonic boost is observed—disappear. This can be seen in the spectral norm plots of Fig. 3.

The lattice harmonic behavior described by the spectral norm of $[M(f)]^{-1}$ also depends on the distribution of the inductor and capacitor values across the lattice. The design of desired inductor and capacitor values, tailored to a specific harmonic amplification performance, is a separate topic, beyond the scope of this paper. However, nonuniformity due to inductor and capacitor imperfections can be studied. Such lattices can be modeled by adding a random number, uniformly distributed in $[-\tau, \tau]$, to the component values L, C_o (where τ denotes the respective tolerance). The spectral norm plots of Fig. 4 demonstrate the effect of component imperfections on the lattice harmonic behavior. Based on these plots, it is clear that for component

[1]The spectral norm for a square matrix M is defined as $\|M\|_2 = \sqrt{\max \text{eigenvalue of } M^H M}$. The spectral norm of a square matrix M^{-1} satisfies $\|M^{-1}\|_2 = \max\{\|M^{-1}x\|_2 : \|x\|_2 = 1\}$.

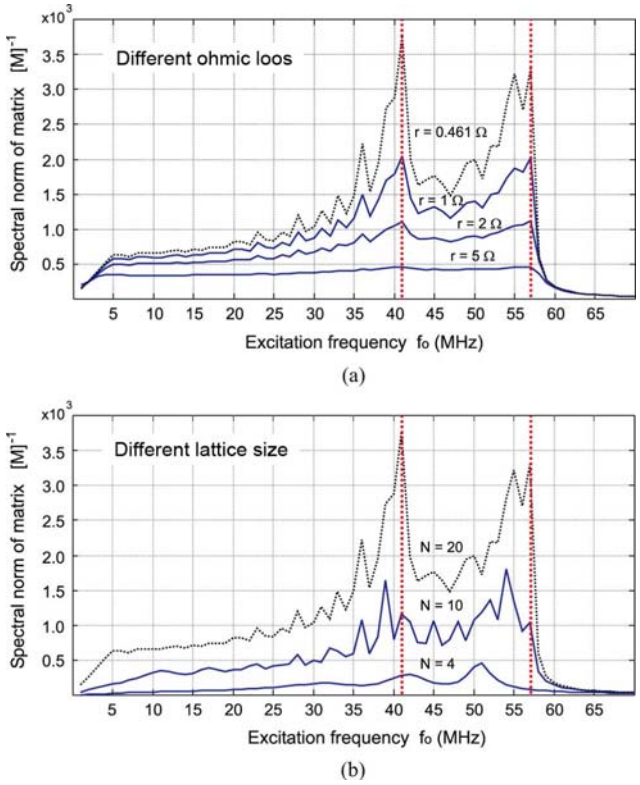

Fig. 3. Spectral norm of $[M(f)]^{-1}$ as a function of excitation frequency. (a) Lattices with inductors of different ohmic losses. Dotted line $r = 0.461\ \Omega$ (implemented example). Solid lines $r = 1\ \Omega$, $2\ \Omega$, and $5\ \Omega$ (other test cases). (b) Lattices of different sizes. Dotted line $N = 20$ (implemented example). Solid lines $N = 10$ and 4 (other test cases).

TABLE I
LATTICE PARAMETERS

Total number of nodes	$20 \times 20 = 400$
Inductance	$L = 380$ nH
Inductance resistance	$r = 0.461$ Ohm
Boundary resistance	$r_b = 57$ Ohm
Zero voltage capacitance	$C_o = 162$ pF
Average capacitance	$\bar{C} = 144$ pF at V=200 mV
Nonlinear coefficient	$b = 0.2823$

tolerances greater than 10%, the range of frequencies in which the spectral norm of $[M(f)]^{-1}$ obtains a relatively large value changes unpredictably [see Fig. 4(b) and (c)], making it hard to identify potential fundamental frequencies generating large harmonic boost.

E. IHG Method

The IHG method uses the spectral norm values of $[M(f)]^{-1}$ to identify excitation frequencies causing intense harmonic boost. The IHG method is divided into the following two steps.

(s1) Calculate the spectral norm $\|[M(f)]^{-1}\|_2$, which is a function of the input frequency f. Identify M frequencies $f_1^* < \cdots < f_M^*$, at which $\|[M(f)]^{-1}\|_2$ is maximized.

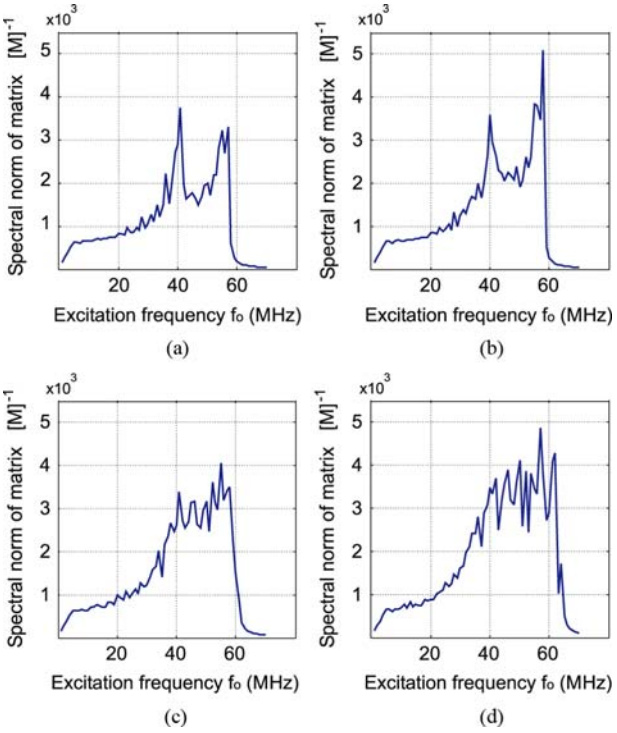

Fig. 4. Spectral norm of $[M(f)]^{-1}$ as a function of excitation frequency for the implemented lattice with components of: (a) zero tolerance (ideal), (b) $\pm 10\%$ tolerance, (c) $\pm 20\%$ tolerance, and (d) $\pm 30\%$ tolerance.

(s2) For a given "M-plet" $\{n_1, \ldots, n_M\} \subset \mathbb{N}^M$, with $n_1 < \cdots < n_M$, the associated promising frequency for IHG, $f_{n_1,\ldots,n_M}$, is given by

$$f_{n_1,\ldots,n_M} = \min_{f \in R} |D_{n_1,\ldots,n_M}(f)|, \tag{13}$$

where $D_{n_1,\ldots,n_M}(f) = \sum_{m=1}^{M} |f_m^* - n_m f|$ is a measure of distance between the harmonics $n_m f$ and the frequencies f_m^*'s found in (s1).

Intuitively, the IHG method attempts to find a fundamental frequency f, the harmonics of which $(n_m f)$ are close to the frequencies f_m^*'s of the lattice. The efficiency of this method will be verified in Section III.

III. IHG METHOD VERIFICATION

The IHG method is applied to a large variety of nonlinear lattices to verify its efficiency. Both numerical simulation with MATLAB and experimental measurement on PCB show excellent agreement with the IHG method prediction.

A. Simulated Tests

Numerical simulations are performed on a 20×20 lattice, and are characterized by four parameters N (number of nodes), C_o (zero-voltage capacitance), L (inductance), and b (nonlinear coefficient). The lattice is excited with $0.4\ V_{pp}$ sinusoidal voltage sources on the bottom and left sides, as in Fig. 1. To verify the generality of the IHG method, different lattices are examined by changing one of the four parameters while

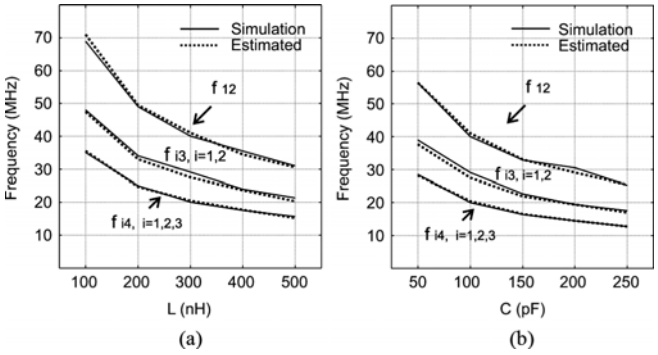

Fig. 5. Frequency estimation. (a) Variable inductance ($C = 100$ pF, $N = 20$, $b = 0.28$). (b) Variable capacitance ($L = 300$ nH, $N = 20$, $b = 0.28$).

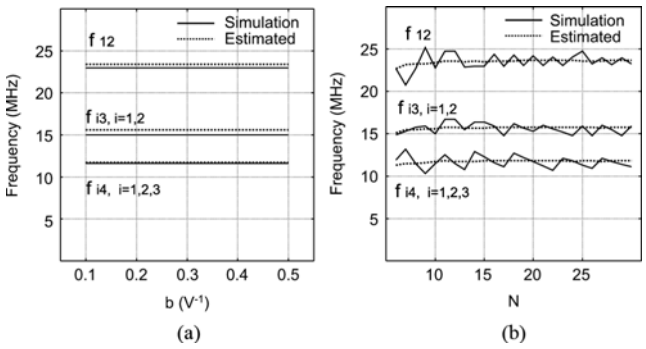

Fig. 6. Frequency estimation. (a) Variable b ($L = 300$ nH, $C = 300$ pF). (b) Variable N ($L = 300$ nH, $C = 300$ pF).

keeping the other three constant. Specifically, L, C_o, b, and N are swept as follows.

- $L = 100{,}200, \ldots, 500$ nH; ($C_o = 300$ pF; $b = 0.28\ V^{-1}$ $N = 20$).
- $C_o = 50{,}100, \ldots, 250$ pF; ($L = 300$ nH; $b = 0.28\ V^{-1}$ $N = 20$).
- $b = 0.1, 0.2, \ldots, 0.5\ V^{-1}$; ($C_o = 300$ pF; $L = 300$ nH; $N = 20$).
- $N = 6, 7, \ldots, 30$; ($C_o = 300$ pF; $L = 300$ nH; $b = 0.28\ V^{-1}$).

The steps of the numerical tests performed in each of the above scenarios are as follows.

(s1) Calculation of:
  (a) The harmonic vectors $\{\hat{h}_k\}$ using (5) and (10) for input fundamental frequency f_0.
  (b) The harmonic energy given by the sum (12), up to $K = 6$ for frequency f_0. Higher order harmonics were omitted as their amplitudes are negligible.

(s2) Repetition of (s1) with f_0 in a wide frequency band (0 up to the cutoff frequency) appropriately selected to capture all variations of $H(f_0)$.

(s3) Selection of frequencies f_0^* of IHG as the ones that locally maximize the harmonic energy, i.e.,

$$f_0^* = \arg\max_{f_0} H(f_0). \tag{14}$$

The IHG method is carried out in the following way.

None in (s1), two lattice modes f_1^* and f_2^* are identified. Following (s2), and according to (13), promising frequencies are estimated for several "2-Plets" as follows:

$$f_1^{\text{est}} = f_{i4} i = 1, 2, 3.$$
$$f_2^{\text{est}} = f_{i3} i = 1, 2.$$
$$f_3^{\text{est}} = f_{12}.$$

We compare these estimated frequencies f_k^{est} given by the IHG method with the frequencies f_0^* locally maximizing the lattice harmonic energy given by (14). These comparisons are displayed in Figs. 5 and 6. The efficiency and generality of the IHG method is clearly shown by the agreement between prediction and actual values in all cases.

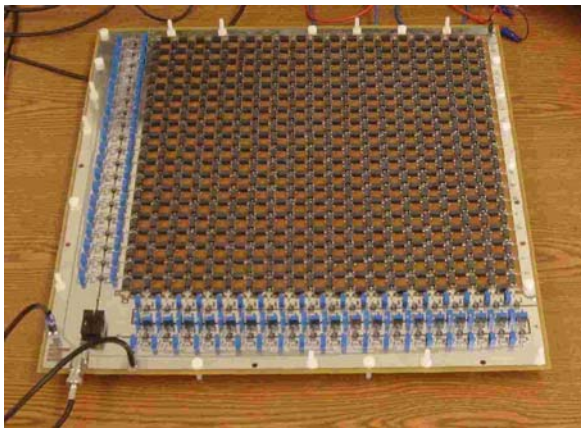

Fig. 7. Photograph of the *LC* lattice.

B. Experiment on PCB

A 20×20 nonlinear *LC* lattice is implemented on PCB (Fig. 7), characterized by the parameters listed in Table I. The promising input frequencies for this lattice are calculated based on the IHG method. These frequencies are compared with frequencies derived by experimental voltage measurements. For this lattice, the spectral norm of matrix $[M(f)]^{-1}$ is plotted as a function of the excitation frequency f_o in Fig. 3. Two frequencies can be identified, at which the spectral norm is locally maximized, i.e., $f_1^* = 41$ MHz and $f_2^* = 57$ MHz. The distance measures $D_{n_1,n_2}(x)$ are calculated according to the IHG method, for several pairs $\{n_1, n_2\}$ with $1 \leq n_1 < n_2 < 5$. The results are plotted in Fig. 8. According to the plots of Fig. 8, the minima of the distance measures reveal estimates of promising input frequencies $f_1^{\text{est}} = f_{i4} = 14.2$ MHz, $i = 1, 2, 3$, $f_2^{\text{est}} = f_{i3} = 19$ MHz, $i = 1, 2$, and $f_3^{\text{est}} = f_{12} = 28.5$ MHz.

The results of the IHG method are verified by performing the simulation steps described in Section III. Three candidate frequencies (close to the previous estimated frequencies) were obtained this way: $f_1^{\text{sim}} = 14.1$ MHz, $f_2^{\text{sim}} = 17.2$ MHz, and $f_3^{\text{sim}} = 28$ MHz.

To verify this prediction, the lattice is excited at the bottom and left side (Fig. 7) by in-phase sinusoidal sources with amplitude 1 V_{pp} frequency varying in the range 1–70 MHz. All capacitors are biased at $V_{\text{off}} = 200$ mV, which gives the steepest capacitance descent $b = 0.28$. The node with the maximum response is selected as the output node, which, by symmetry,

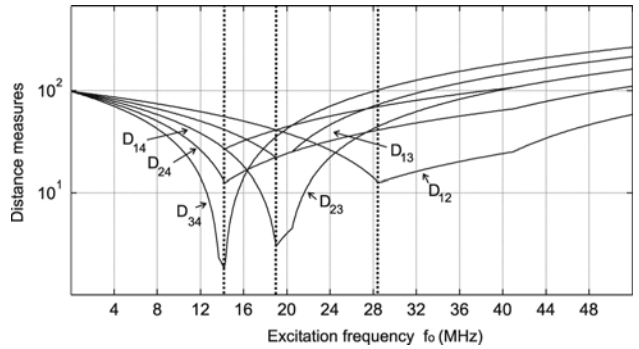

Fig. 8. Distance measure functions as a function of the fundamental frequency.

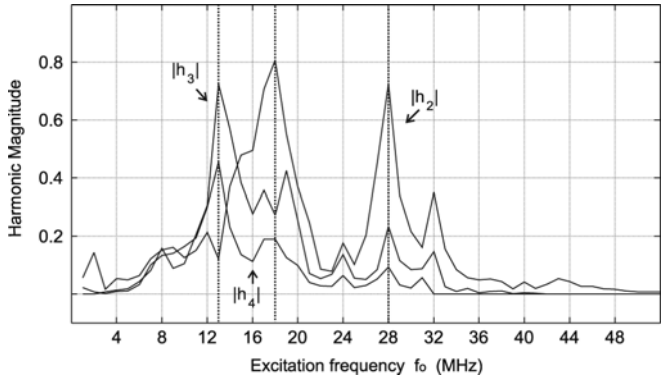

Fig. 9. Experimental results: Magnitude of the second, third, and fourth harmonics as a function of the fundamental frequency $f_o = 1, 2, \ldots, 52$ MHz.

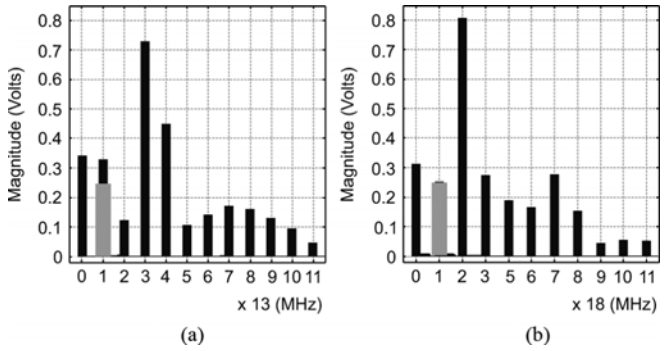

Fig. 10. Optimal lattice responses for different excitation frequencies (grey bars) compared with lattice input (black bar). (a) Third and fourth harmonic boost of fundamental 13 MHz. (b) Second harmonic boost of fundamental 18 MHz.

turns out to be the central node $(9, 9)$. The amplitudes of the second, third, and fourth harmonics are plotted in Fig. 9, each curve depicting the amplitude of one harmonic at different input frequencies $f_o = 1, 2, \ldots, 52$. It is shown that the nonlinear *LC* lattice generates large harmonics for a certain input frequency range, i.e., 7–30 MHz. Specifically, at $f_1^{\text{exp}} = 13$ MHz $f_2^{\text{exp}} = 18$ MHz and $f_3^{\text{exp}} = 28$ MHz, the third, second, and fourth harmonics are maximized, respectively. The spectra of the output at $f_1^{\text{exp}} = 13$ MHz and $f_2^{\text{exp}} = 18$ MHz inputs are displayed in Fig. 10, which shows rich harmonic generation at these frequencies. Table II summarizes the results of the simulation, estimation, and experiments, showing frequencies at which intense harmonic boost occurs.

TABLE II
FREQUENCIES OF INTENSE HARMONIC BOOST

Simulation f^{sim}	IHG method f^{est}	Experiment f^{exp}
14.1 MHz	14.2 MHz	13.0 MHz
17.2 MHz	19.0 MHz	18.0 MHz
28.0 MHz	28.5 MHz	28.0 MHz

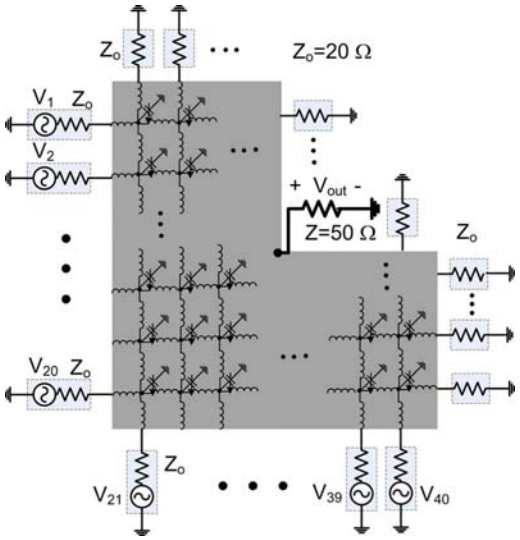

Fig. 11. Schematic of a nonlinear *LC* lattice in a CMOS process.

In conclusion, extensive numerical simulations and experimental measurements show that the IHG method is an effective method for determining optimal excitation frequencies that result in IHG.

IV. CMOS IMPLEMENTATION OF NONLINEAR *LC* LATTICE

In order to examine the performance of this lattice topology in the terahertz frequency range, a 20×20 lattice using a standard 0.13-μm CMOS process is designed and simulated. Fig. 11 shows the schematic of this lattice.

Multiple synchronous signal sources driving the left and bottom side of the lattice to generate two planar wavefronts. To make these signals sources, a tree-like distribution network along with matching networks at each junctions is designed. This network connects an external 50-GHz source to a series of small amplifiers at each node. The output node is at the center of the lattice and is matched to 50 Ω. To make this node more accessible, the upper right corner of the lattice is removed. The entire top and left boundary nodes are terminated with a resistor matched to the local impedance at that node. This will eliminate any reflection from the boundaries that can interference with the incoming waves from the sources.

All inductors are implemented using a 30-μm coplanar waveguide with total inductance of 15 pH. Fig. 12 shows the simulated quality factor of this inductor using Ansoft Technologies' High Frequency Structure Simulator (Ansoft HFSS). The varactors are designed using an accumulation mode nMOSVAR with average capacitance of 150 fF [37], [38]. Fig. 13(a) shows the characteristic of the accumulation-mode nMOSVAR used

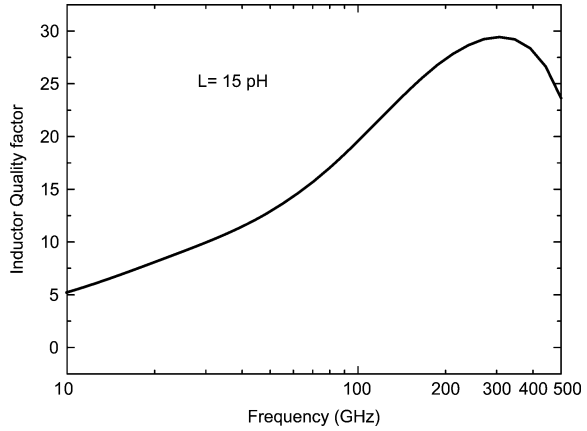

Fig. 12. Simulated quality factor of each inductor.

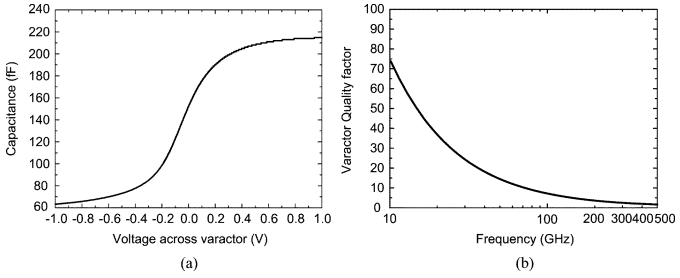

Fig. 13. Simulated characteristic of the nonlinear capacitor used to build the lattice in a 130-nm CMOS process. (a) Characteristic of MOSVAR used in the nonlinear lattice. (b) Quality factor of each nMOSVAR.

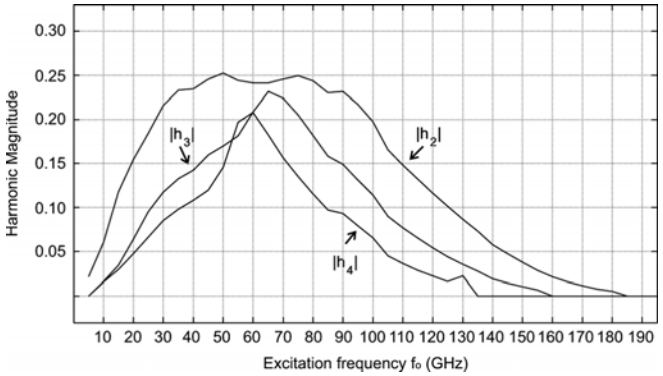

Fig. 14. Simulation results: Magnitude of the second, third, and fourth harmonics as a function of the fundamental frequency f_o. X-axis: excitation frequency. Y-axis: harmonic magnitude.

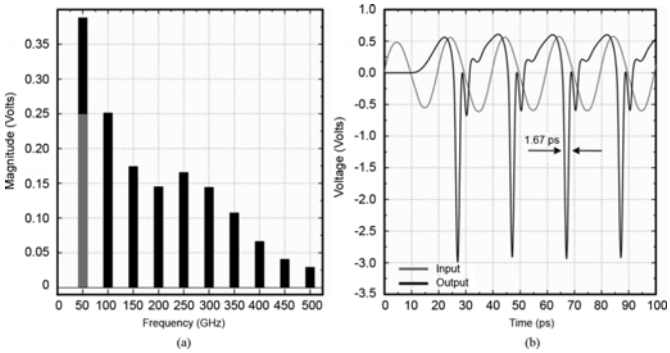

Fig. 15. Simulated lattice response at input frequency 50-GHz: input (grey) and output (black). (a) Frequency-domain response. (b) Time-domain response.

in this design, and Fig. 13(b) shows its quality factor as a function of frequency. The ratio between minimum and maximum capacitances is around 3, which determines the nonlinearity of the lattice. Similar to [38], the varactors use a multifinger structure. The size and number of fingers is selected for a maximum nonlinearity and minimum series resistance. By carefully optimizing the geometry of these varactors an *RC* cutoff frequency of more than 150 GHz is achieved. To achieve the lowest pulsewidth at the output of the nonlinear lattice, it is necessary to carefully select the varactor bias point. In general, this may be an additional constraint in system design since it will require additional dc level shifting to adjust the input levels. Nonetheless, this level of signal conditioning is easily achieved in today's integrated circuits. In our design, this optimal bias point is around 0 V since at this point the *C/V* curve shown in Fig. 13(a) has the highest slope. As a result, all MOSVARs are connected to a ground plane, which simplifies the layout and fabrication.

Based on the inductance and average capacitance values, the cutoff frequency of the lattice is 300 GHz. The output is measured at the center of the lattice with a 50-Ω termination. All circuit simulations are performed using Cadence Spectre.

Fig. 14 shows the lattice response for different inputs characterized by variable frequency and fixed amplitude at 0.5 V. The generation of the second, third, and fourth harmonics is maximized for input frequencies in the range of 50–70 GHz. Due to the nonlinearity, the energy of the fundamental frequency is converted into high-order harmonic components. However, the frequency-dependent loss of the inductors due to skin effects and substrate couplings, as well as the limited *C/V* swing range of the nMOS varactors, limit further amplification of the generated harmonics. Based on Fig. 14, the harmonic generation stops for input frequencies greater than half of the cutoff frequency $(\approx 150\ \text{GHz})$.

It appears that the total energy of the generated harmonic components is maximized for 50-GHz sinusoidal input. The magnitudes of the harmonics of the node with the maximum response for this input frequency are displayed in Fig. 15(a). The nonlinearity of the lattice generates large components at 400 GHz, which is around three times more than the cutoff frequency of the fastest active device in this process. Fig. 15(b) shows the time-domain input and output waveforms measured at the center of the lattice for 50-GHz sinusoidal inputs. Due to the nonlinear constructive interference, the output peak-to-peak amplitude is higher than 3 V, which is three times greater than the input amplitude. The half amplitude pulsewidth of the output waveform is as narrow as 1.67 ps. This is the largest reported amplitude of such narrow pulses generated on a silicon process.

Lattices of different dimensions, capacitance (C_o), and inductance (L) values excited at 50 GHz are also simulated. Fig. 16(a) displays the magnitude of the first, second, and third harmonics of the lattice response for different values of N varying from 5 to 35. According to this figure, the harmonic boost is maximized when $20 \leq N \leq 25$. For $N < 20$, the nonlinear wave combining is less intense, resulting in degraded harmonic generation. On the other hand, for $N > 25$, the harmonic magnitudes of the lattice response are attenuated

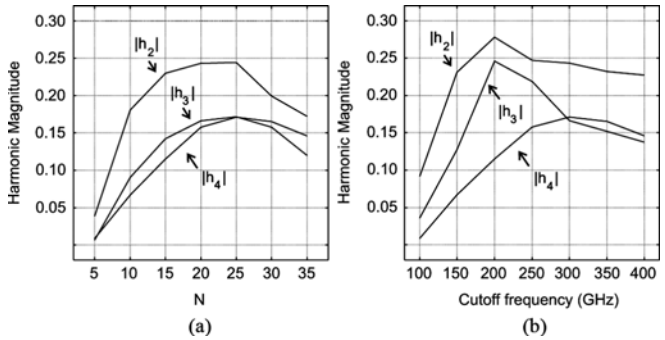

Fig. 16. Harmonic magnitude for 50-GHz input. (a) As a function of the lattice size N (cutoff frequency $= 300$ GHz). (b) As a function of the cutoff frequency ($N = 25$).

due to the accumulated loss by the increased number of lattice sections. Fig. 16(b) displays the magnitude of the first, second, and third harmonics of the lattice response for different capacitance and inductance values, or equivalently, different cutoff frequencies (the cutoff frequency is inversely proportional to the square root of the product of the inductance and capacitance values [25]). As the inductance and capacitance values increase (equivalently, as the cutoff frequency decreases), the input frequencies of intense harmonic response become smaller, a fact that is also indicated by the plots of Fig. 5. For lattices with cutoff frequencies different (bigger/smaller) than 300 GHz, IHG appears at frequencies different (bigger/smaller) than 50 GHz. Due to this effect, the harmonic response of such lattices at 50 GHz is degraded as displayed in Fig. 16(b).

V. Conclusions

The behavior of 2-D nonlinear inductor–capacitor lattices is studied from a spectral point of view; perturbative solutions for the harmonic response of these lattices are derived for arbitrary-order polynomial nonlinearities. It is verified by simulations, as well as experimental measurements that intense harmonic amplification is observed when either the fundamental, or one of its harmonics, is close to frequencies, which maximize locally the spectral norm values of the lattice response matrix. As a result, the IHG method is introduced. This method seeks to minimize the total distance between two sets of frequencies, which are: 1) the frequencies at which the spectral norm of the lattice response matrix is locally maximized and 2) the excitation frequency and its harmonics. Nonuniform distributions of inductance and capacitance values, the lattice size, as well as the inductor ohmic losses all affect the spectral norm of the lattice response matrix, and, as a result, the lattice harmonic performance. Although designing nonuniform lattices to improve the lattice harmonic response appears to be a difficult task, reducing the inductor losses or developing highly nonlinear capacitive elements are simple first steps towards implementing these topologies for intense harmonic amplification. Simulations using a 0.13-μm CMOS process demonstrated harmonic generation at frequencies three times the cutoff frequency of the fastest device in this process, indicating potential extensions to terahertz range applications.

Appendix

In order to study nonlinear wave interactions in a general $N \times N$ *LC* lattice, we have to express the coupled governing current/voltage equations at the *LC* element level. These are the Kirchhoff voltage and current laws. At node i, j, these laws give the system

$$\begin{aligned}\frac{\partial}{\partial t}\int_{V_{i,j}} C_{ij}(V_{ij})dV_{i,j} &= I^H_{i,j} + I^V_{i,j} - I^H_{i,j+1} - I^H_{i+1,j}\\ L^H_{i,j}\frac{\partial I^H_{i,j}}{\partial t} &= V_{i,j} - V_{i,j-1} - rI^H_{i,j}\\ L^V_{i,j}\frac{\partial I^V_{i,j}}{\partial t} &= V_{i,j} - V_{i-1,j} - rI^V_{i,j}\end{aligned} \tag{15}$$

where C_{ij}, $L^H_{i,j}$, and $L^V_{i,j}$ are, respectively, the capacitance and horizontal/vertical inductances of the *LC* element at node i, j. The fact that the inductors are nonideal is modeled by a small ohmic resistance r. The node voltage and the flowing currents in the horizontal and vertical inductor of the *LC* element i, j are denoted by $V_{ij}, I^H_{i,j}$ and $I^V_{i,j}$.

For small perturbations around a fixed voltage value, a first-order dependence of capacitance on the observed voltage value at the node i, j can be assumed, i.e.,

$$C_{i,j}(V_{i,j}) = C_o(1 - bV_{i,j}). \tag{16}$$

Applying (16) to the element equations (15) leads to

$$\begin{aligned}C_o\frac{\partial V_{ij}}{\partial t} &= I^H_{i,j} + I^V_{i,j} - I^H_{i,j+1} - I^H_{i+1,j} + bC_oV_{i,j}\frac{\partial V_{i,j}}{\partial t}\\ L^H_{i,j}\frac{\partial I^H_{i,j}}{\partial t} &= V_{i,j} - V_{i,j-1} - rI^H_{i,j}\\ L^V_{i,j}\frac{\partial I^V_{i,j}}{\partial t} &= V_{i,j} - V_{i-1,j} - rI^V_{i,j}.\end{aligned} \tag{17}$$

A mapping from the "local" node coordinates (i, j) to a "global" system index k and a corresponding state vector are defined as follows:

$$\begin{aligned}k &= i + (j-1)N\\ (i,j) &\in \{1,\ldots,N\}\times\{1,\ldots,N\}, \quad k \in \{1,\ldots,N^2\}\end{aligned} \tag{18}$$

$$\{s\} = \{V_{1,1},\ldots,V_{N,N},I^H_{1,2},\ldots,I^H_{N,N},I^V_{2,1},\ldots,I^V_{N,N}\}. \tag{19}$$

In order to derive a global system based on (17), we have to define the following source voltage vector $\{x\}$ and boundary currents according to Fig. 17:

$$\begin{aligned}\{x\} &= \{x^{HV}, 0_{1:N(N-1)}, 0_{1:N(N-1)}\}\\ \{x^{HV}\} &= \{x^V, x^H\}\\ \{x^V\} &= \frac{1}{r_s}\{0, X^V_{1:N-1}\}\\ \{x^H\} &= \frac{1}{r_s}\{X^H_1, 0_{1:(N-1)},\ldots, X^H_N, 0_{1:(N-1)}\}\end{aligned} \tag{20}$$

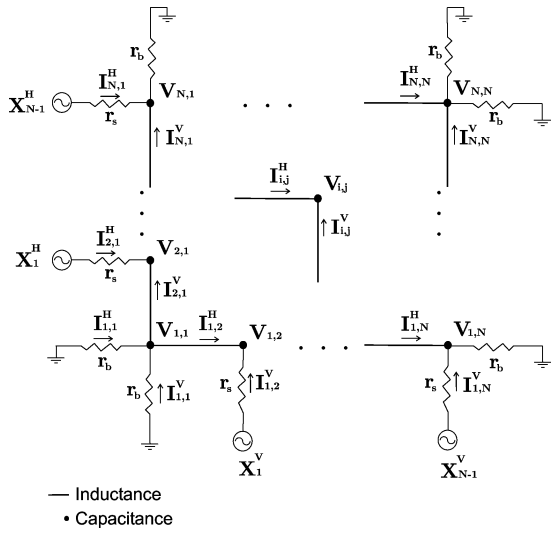

Fig. 17. Modeling of 2-D *LC* lattice.

$$
\begin{aligned}
I^H_{1,1} &= -\frac{V_{1,1}}{r_b}\; i=\{1,\ldots,N\}\\
I^V_{1,1} &= -\frac{V_{1,1}}{r_b}\; i=\{1,\ldots,N\}\\
I^H_{i,N+1} &= \frac{V_{i,N}}{r_b}\; i=\{1,\ldots,N\}\\
I^V_{N+1,i} &= \frac{V_{N,i}}{r_b}\; i=\{1,\ldots,N\}\\
I^H_{i+1,1} &= \frac{X^H_i - V_{i+1,1}}{r_s}\; i=\{1,\ldots,N-1\}\\
I^V_{1,j+1} &= \frac{X^V_j - V_{1,j+1}}{r_s}\; j=\{1,\ldots,N-1\}
\end{aligned}
\tag{21}
$$

where r_b is the boundary termination resistance of the lattice and r_s is the source resistance. The boundary vector $\{x\}$ contains the external voltage source values. Given the boundary conditions of (20) and (21), system (17) can be assembled in a global system

$$
[E]\left\{\frac{\partial s}{\partial t}\right\} = [F]\{s\} + \{x\} + b[C]\{s\}.\left\{\frac{\partial s}{\partial t}\right\} \tag{22}
$$

where $[E]$ is a diagonal matrix containing the capacitance C_o and inductance values $L^H_{i,j}$, $L^V_{i,j}$, and $[F]$ is a sparse matrix containing $1, -1, -r, -1/r_b, -2/r_b$, and $-1/r_s$ values depending on the lattice node connections (Fig. 17)

$$
[F] = \begin{bmatrix} F_{11} & F_{12} & F_{13} \\ -F_{12}^T & -rI_{M\times M} & 0_{M\times M} \\ -F_{13}^T & 0_{M\times M} & -rI_{M\times M} \end{bmatrix} \tag{23}
$$

$$
\begin{aligned}
[F_{11}] &= \left[\mathrm{diag}(\{f^a_{11}\},\{f^b_{11}\},\ldots,\{f^b_{11}\},\{f^c_{11}\})\right]\\
\{f^a_{11}\} &= \left\{-\frac{2}{r_b}, -\frac{1}{r_s}(1_{N-2}), -\frac{1}{r_b}-\frac{1}{r_s}\right\}\\
\{f^b_{11}\} &= \left\{-\frac{1}{r_s}, (0_{N-2}), -\frac{1}{r_b}\right\}\\
\{f^c_{11}\} &= \left\{-\frac{1}{r_b}-\frac{1}{r_s}, -\frac{1}{r_b}(1_{N-2}), -\frac{2}{r_b}\right\}
\end{aligned}
$$

$$
\begin{aligned}
[F_{12}] &= \begin{bmatrix} f_{12} & 0_{N\times N-1} & 0_{N\times N-1} \\ \ldots & \ldots & \ldots \\ 0_{N\times N-1} & 0_{N\times N-1} & f_{12} \end{bmatrix}\\
[f_{12}] &= \begin{bmatrix} -1 & 0 & 0 & \ldots & 0 \\ 1 & -1 & 0 & \ldots & 0 \\ 0 & 1 & -1 & \ldots & 0 \\ \ldots & \ldots & \ldots & \ldots & -1 \\ 0 & 0 & 0 & \ldots & 1 \end{bmatrix}_{N\times N-1}\\
[F_{13}] &= \begin{bmatrix} -I_{N\times N} & 0_{N\times N} & 0_{N\times N} & \ldots & 0_{N\times N} \\ I_{N\times N} & -I_{N\times N} & 0_{N\times N} & \ldots & 0_{N\times N} \\ \ldots & \ldots & \ldots & \ldots & \ldots \\ 0_{N\times N} & \ldots & \ldots & \ldots & -I_{N\times N} \\ 0_{N\times N} & \ldots & \ldots & \ldots & I_{N\times N} \end{bmatrix}.
\end{aligned}
\tag{24}
$$

Assuming $M = N(N-1)$, $[C]$ is the following capacitance matrix:

$$
[C] = \begin{bmatrix} C_o I_{N^2\times N^2} & 0_{N^2\times M} & 0_{N^2\times M} \\ 0_{M\times N^2} & 0_{M\times M} & 0_{M\times M} \\ 0_{M\times N^2} & 0_{M\times M} & 0_{M\times M} \end{bmatrix}. \tag{25}
$$

In order to solve perturbatively for the vector $\{s\}$, we have to express $\{s\}$ as a power series in the nonlinear coefficient b

$$
\{s\} = \{s_0\} + b\{s_1\} + b^2\{s_2\} + \cdots. \tag{26}
$$

Plugging (26) into (22) and isolating the coefficients of the powers of b leads to

$$
[A_0(s_0)] + b[A_1(s_0,s_1)] + b^2[A_2(s_0,s_1,s_2)] + \cdots = 0 \tag{27}
$$

where A_k is an expression that depends on the vectors $\{s_0\},\ldots,\{s_k\}$

$$
\begin{aligned}
&A_0(s_0)\\
&\quad = [E]\left\{\frac{\partial s_0}{\partial t}\right\} - [F]\{s_0\} - \{x\}\\
&A_n(s_0,\ldots,s_n)\\
&\quad = [E]\left\{\frac{\partial s_n}{\partial t}\right\} - [F]\{s_n\} - [C]\sum_{k=1}^{n-1}\{s_k\}.\left\{\frac{\partial s_{n-1-k}}{\partial t}\right\}.
\end{aligned}
\tag{28}
$$

In order for (27) to be true for every value of b, all the expressions A_n, $n = 0,1,2,\ldots$ must be equal to zero, i.e.,

$$
\begin{aligned}
[E]\left\{\frac{\partial s_0}{\partial t}\right\} &= [F]\{s_0\} - \{x\}\\
[E]\left\{\frac{\partial s_n}{\partial t}\right\} &= [F]\{s_n\} - [C]\sum_{k=1}^{n-1}\{s_k\}.\left\{\frac{\partial s_{n-1}}{\partial t}\right\}.
\end{aligned}
\tag{29}
$$

Taking the Fourier transform of the last set of equations leads to the following system:

$$
\begin{aligned}
\{\hat{s}_0\} &= (j(2\pi f)[E] - [F])^{-1}\{\hat{x}\}\\
\{\hat{s}_n\} &= (j(2\pi f)[E] - [F])^{-1}[C]\sum_{k=1}^{n-1}\{\hat{s}_k\} * \{j(2\pi f)\hat{s}_{n-1-k}\}.
\end{aligned}
\tag{30}
$$

Here, the element-by-element multiplication in the time domain is replaced by convolution in the frequency domain.

ACKNOWLEDGMENT

The authors would like to thank O. Momeni, Y. Tousi, and M. Adnan, all with Cornell University, Ithaca, NY, for helpful discussions regarding various aspects of this work. The authors also acknowledge M. Azarmnia and H. Yu for their support.

REFERENCES

[1] P. H. Siegel, "Terahertz technology," *IEEE Trans. Microw. Theory Tech.*, vol. 50, no. 3, pp. 910–928, Mar. 2002.

[2] D. W. Van der Weide, J. Murakowski, and F. Keilmann, "Gas-absorption spectroscopy with electronic terahertz techniques," *IEEE Trans. Microw. Theory Tech.*, vol. 48, no. 4, pp. 740–743, Apr. 2000.

[3] Z. Jiang and X. Zhang, "Terahertz imaging via electrooptic effect," *IEEE Trans. Microw. Theory Tech.*, vol. 47, no. 12, pp. 2644–2650, Dec. 1999.

[4] R. Piesiewicz, T. K. Ostmann, N. Krumbholz, D. Mittleman, M. Koch, J. Schoebel, and T. Kurner, "Short-range ultra-broadband terahertz communications: Concepts and perspectives," *IEEE Antennas Propag. Mag.*, vol. 49, no. 6, pp. 24–39, Dec. 2007.

[5] C. F. Jou, W. W. Lam, H. Z. Chen, K. S. Stolt, N. C. Luhmann, and D. B. Rultedge, "Millimeter-wave diode-grid frequency doubler," *IEEE Trans. Microw. Theory Tech.*, vol. 36, no. 11, pp. 1507–1514, Nov. 1988.

[6] J. Mateu, C. Collado, N. Orloff, J. C. Booth, E. Rocas, A. Padilla, and J. M. O'Callaghan, "Third-order intermodulation distortion and harmonic generation in mismatched weakly nonlinear transmission lines," *IEEE Trans. Microw. Theory Tech.*, vol. 57, no. 1, pp. 10–18, Jan. 2009.

[7] C. C. H. Tang, "An exact analysis of varactor frequency multipliers," *IEEE Trans. Microw. Theory Tech.*, vol. MTT-14, no. 4, pp. 210–212, Apr. 1966.

[8] J. Stake, S. H. Jones, L. Dillner, S. Hollung, and E. L. Kollberg, "Heterostructure-barrier-varactor design," *IEEE Trans. Microw. Theory Tech.*, vol. 48, no. 4, pp. 677–682, Apr. 2000.

[9] X. Oriols and F. Martin, "Analytical solitons in nonlinear transmission lines loaded with heterostructura barrier varactors," *J. Appl. Phys.*, vol. 90, no. 5, pp. 2595–2600, Sep. 2001.

[10] F. Martin and X. Oriols, "A simple model to study soliton wave propagation in periodically loaded nonlinear transmission line," *Appl. Phys. Lett.*, vol. 78, no. 18, pp. 2802–2804, Apr. 2001.

[11] R. Landauer, "Shock waves in nonlinear transmission lines and their effect on parametric amplification," *IBM J. Res. Develop.*, no. 4, pp. 391–401, Oct. 1960.

[12] R. Hirota and K. Suzuki, "Studies on lattice solitons by using electrical networks," *J. Phys. Soc. Jpn.*, vol. 28, pp. 1366–1367, 1970.

[13] K. S. Champlin and D. R. Singh, "Small-signal second-harmonic generation by a nonlinear transmission line," *IEEE Trans. Microw. Theory Tech.*, vol. MTT-34, no. 3, pp. 351–353, Mar. 1986.

[14] H. Ikezi, S. S. Wojtowicz, R. E. Waltz, and D. R. Baker, "High-power soliton generation at microwave frequencies," *J. Appl. Phys.*, vol. 64, no. 6, pp. 3277–3281, Sep. 1988.

[15] M. Li, K. Krishnamurthi, and R. G. Harrison, "A fully distributed heterostructure-barrier varactor nonlinear transmission-line frequency multiplier and pulse sharpener," *IEEE Trans. Microw. Theory Tech.*, vol. 46, no. 12, pp. 2295–2301, Dec. 1998.

[16] J. Duchamp, P. Ferrari, M. Fernandez, A. Jrad, X. Melique, J. Tao, S. Arscott, D. Lippens, and R. G. Harrison, "Comparison of fully distributed and periodically loaded nonlinear transmission lines," *IEEE Trans. Microw. Theory Tech.*, vol. 51, no. 4, pp. 1105–1116, Apr. 2003.

[17] E. Lheurette, M. Fernandez, X. Melique, P. Mounaix, O. Vanbesien, and D. Lippens, "Non linear transmission line quintupler loaded by heterostructure barrier varactors," in *Proc. Eur. Microw. Conf.*, Munich, Germany, Oct. 1999, pp. 217–220.

[18] D. Jager, "Characteristics of travelling waves along the nonlinear transmission lines for monolithic integrated circuits: A review," *Int. J. Electron.*, vol. 58, no. 4, pp. 649–669, Apr. 1985.

[19] J. R. Thorpe, P. Steenson, and R. Miles, "Non-linear transmission lines for millimiter-wave frequency multiplier applications," in *Proc. 6th IEEE Int. Terahertz Electron. Conf.*, New York, New York, 1998, pp. 54–57.

[20] E. Carman, M. Case, M. Kamegawa, R. Yu, K. S. Giboney, and M. J. W. Rodwell, "V-band and W-band broad-band, monolithic distributed frequency multipliers," *IEEE Microw. Guided Wave Lett.*, vol. 2, no. 6, pp. 253–254, Jun. 1992.

[21] M. J. W. Rodwell, M. Kamegawa, R. Yu, M. Case, E. Carman, and K. S. Giboney, "GaAs nonlinear transmission lines for picosecond pulse generation and millimeter-wave sampling," *IEEE Trans. Microw. Theory Tech.*, vol. 39, no. 7, pp. 1194–1204, Jul. 1991.

[22] M. Case, M. Kamegawa, R. Yu, M. J. W. Rodwell, and J. Franklin, "Impulse compression using soliton effects in a monolithic GaAs circuit," *Appl. Phys. Lett.*, vol. 58, no. 2, pp. 173–175, Jan. 1991.

[23] M. Case, E. Carman, R. Yu, M. J. W. Rodwell, and M. Kamegawa, "Picosecond duration, large amplitude impulse generation using electrical soliton effects," *Appl. Phys. Lett.*, vol. 60, no. 24, pp. 3019–3021, Jun. 1992.

[24] X. Melique, A. Maestrini, E. Lheurette, P. Mounaix, M. Favreau, O. Vanbesien, J. M. Goutoule, G. Beaudin, T. Nahri, and D. Lippens, "12% efficiency and 9.5 dBm output power from InP-based heterostructure barrier varactor triplers at 250 GHz," in *IEEE MTT-S Int. Microw. Symp. Dig.*, Anaheim, CA, 1999, pp. 123–126.

[25] E. Afshari and A. Hajimiri, "A non-linear transmission lines for pulse shaping in silicon," *IEEE J. Solid-State Circuits*, vol. 40, no. 3, pp. 744–52, Mar. 2005.

[26] L. Brillouin, *Wave Propagation in Periodic Structrures: Electric Filters and Crystal Lattices*. New York: Dover, 1953.

[27] J. N. Dinkel, C. Setzer, S. Rawal, and K. E. Lonngren, "Soliton propagation and interaction on a two-dimensional nonlinear transmission line," *Chaos, Solitons, Fractals*, vol. 12, no. 1, pp. 91–96, Jan. 2001.

[28] H. Wang and X. H. Gegenhasi, "2D Toda lattice equation with self-consistent sources: Casoratian type solutions, bilinear Bäcklund transformation and Lax pair," *J. Comput. Appl. Math.*, vol. 202, no. 1, pp. 133–143, May 2007.

[29] K. Maruno and G. Biondini, "Resonance and web structure in discrete soliton systems: The two-dimensional Toda lattice and its fully discrete and ultra-discrete analogues," *J. Phys. A, Math. Gen.*, vol. 37, pp. 11 819–11 839, 2004.

[30] W. S. Duan, "Nonlinear waves propagating in the electrical transmission line," *Europhys. Lett.*, vol. 66, no. 2, pp. 192–197, 2004.

[31] M. M. Lin and W. S. Duan, "Wave packet propagating in an electrical transmission line," *Chaos, Solitons, Fractals*, no. 24, pp. 191–196, Apr. 2005.

[32] E. Kengne, S. T. Chui, and W. M. Liu, "Modulational instability criteria for coupled nonlinear transmission lines with dispersive elements," *Phys. Rev. E, Stat. Phys. Plasmas Fluids Relat. Interdiscip. Top.*, vol. 74, 2006, Art. ID 036614.

[33] E. Afshari, H. S. Bhat, A. Hajimiri, and J. E. Marsden, "Extremely wideband signal shaping using one- and two-dimensional nonuniform nonlinear transmission lines," *J. Appl. Phys.*, vol. 99, 2006, Art. ID 054901.

[34] H. S. Bhat and E. Afshari, "Nonlinear constructive interference in electrical lattices," *Phys. Rev. E, Stat. Phys. Plasmas Fluids Relat. Interdiscip. Top.*, vol. 77, no. 6, pp. 066602-1–066602-13, Jun. 2008.

[35] L. A. Ostroviskii, V. V. Papko, and Y. A. Stepanyants, "Solitons and nonlinear resonance in two-dimensional lattices," *Sov. Phys. JETP*, vol. 51, no. 2, pp. 831–841, Feb. 1980.

[36] Y. A. Stepanyants, "Experiemtnal study of 'Cerenkov' radiation form solitons in two dimensional *LC*-lattices," *Radiophys. Quantum Electron.*, vol. 26, no. 7, pp. 601–607, Jul. 1983.

[37] E. Kameda, T. Matsuda, Y. Emura, and T. Ohzone, "Study of the current-voltage characteristics in MOS capacitors with Si-implanted gate oxide," *Solid State Electron.*, vol. 43, no. 3, pp. 555–63, Mar. 1999.

[38] C.-C. Ho *et al.*, "0.13-μm RF CMOS and varactors performance optimization by multiple gate layouts," *IEEE Trans. Electron Devices*, vol. 51, no. 12, pp. 2181–2185, Dec. 2004.

Georgios N. Lilis (S'08–M'08) received the B.S. degree in electrical engineering from National Technical University of Athens (N.T.U.A), Athens, Greece, in 2002, and the M.S. and Ph.D. degrees in electrical engineering from Cornell University, Ithaca, NY, in 2006 and 2008, respectively.

He was with the Antenna Laboratory, N.T.U.A, during which time he implemented RF switching on multielement antenna modules. In 2004, he joined the Cornell Communications Networks Research Group, Cornell University, and in 2007, he joined the Ultra High-Speed Nonlinear Integrated Circuits Laboratory, Cornell University. His research interests lie in the general area of wave propagation phenomena in various media with a focus on acoustic and electromagnetic implementations.

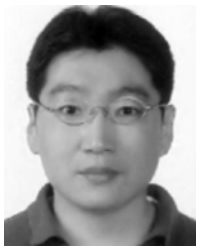

Jihyuk Park received the B.Sc. degree in electrical and computer engineering from Cornell University, Ithaca, NY, in 2007, and is currently working toward the M.Eng. and M.Sc. degrees at Cornell University.

His research interest is RF/analog circuit design in general.

Wooram Lee (S'07) received the B.Sc. and M.S. degrees in electrical engineering from the Korea Advanced Institute of Science and Technology (KAIST), Daejeon, Korea, in 2001 and 2003, respectively, and is currently working toward the Ph.D degree at Cornell University, Ithaca, NY.

From 2003 to 2007, he was a Research Engineer with the Electronics and Telecommunications Research Institute (ETRI), Daejeon, Korea, where he was involved with optical transceivers and links for wavelength division multiplexed passive optical network (WDM-PON). His research interests include high-performance RF integrated circuit (IC) design based on nonlinear electronics for low-noise parametric amplification, oscillation, and terahertz pulse generation.

Mr. Lee was the recipient of the 2007 Samsung Graduate Fellowship and the Best Paper Award of the 2009 IEEE Radar Conference. He was also the Silver Medal recipient of the 1996 National Physics Competition.

Guansheng Li received the B.S. and M.S. degrees in electronics engineering from Tsinghua University, Beijing, China, in 2005 and 2007, respectively, and is currently working toward the Ph.D. degree in electrical and computer engineering at Cornell University, Ithaca, NY.

In 2007, he was named a Jacobs Scholar at Cornell University. He is a Reviewer for *Wireless Communications and Mobile Computing*. His current research is mainly concerned RF IC design with a special interest in multiphase and multiband oscillator design and frequency synthesis. He has also conducted research on wireless communications and networking, studying cross-layer optimization of wireless networks and wireless network coding.

Mr. Li is a reviewer for the IEEE TRANSACTIONS ON WIRELESS COMMUNICATIONS and IEEE SENSORS JOURNAL.

Harish S. Bhat received the A.B. degree in mathematics from Harvard University, Boston, MA, in 2000, and the Ph.D. degree in control and dynamical systems from the California Institute of Technology, Pasadena, in 2005.

He is currently an Assistant Professor with the School of Natural Sciences, University of California, Merced. His broad research interests include applied mathematics with a focus on linear and nonlinear waves.

Ehsan Afshari (S'98–M'07) was born in 1979. He received the B.Sc. degree in electronics engineering from the Sharif University of Technology, Tehran, Iran, in 2001, and the M.S. and Ph.D. degrees in electrical engineering from the California Institute of Technology, Pasadena, in 2003, and 2006, respectively.

In August 2006, he joined the Faculty of Electrical and Computer Engineering, Cornell University, Ithaca, NY.

Prof. Afshari was the recipient of the 2010 National Science Foundation (NSF) CAREER Award, the 2008 Defense Advanced Research Projects Agency (DARPA) Young Faculty Award, and Iran's 2001 Best Engineering Student award by the President of Iran. He was also the recipient of the Best Paper Award of the 2003 Custom Integrated Circuits Conference (CICC), First Place at the 2005 Stanford–Berkeley–California Institute of Technology Inventors Challenge, the Best Undergraduate Paper Award of the 1999 Iranian Conference on Electrical Engineering, the Silver Medal of the 1997 Physics Olympiad, and the 2004 Award of Excellence in Engineering Education of the Association of Professors and Scholars of Iranian Heritage (APSIH).